Coherent population trapping as a magnetic-field diagnostic for hydrogen plasmas

D. R. Farley, J. M. Mitrani, and S. A. Cohen

Princeton Plasma Physics Laboratory, Princeton, New Jersey 08543, USA

Coherent population trapping (CPT) is theoretically examined as a magnetic-field diagnostic for high-β hydrogen plasma. Time-dependent quantum mechanical Bloch equations, which describe the evolution of the $2s$ and $3p$ level populations of the hydrogen atom under CPT conditions, were solved numerically. When the frequency difference of two copropagating lasers equals the energy difference between the atoms' levels subject to the local magnetic field, a discernable CPT dark line in the Hα emission is predicted, enabling the possibility of noninvasive, localized magnetic-field measurements. The effects of fine and hyperfine level structure, Doppler broadening, plasma-generated electric fields, and degree-of-hydrogen ionization are included in the model. A shift in dark-line position of 15% of the linewidth is predicted to be caused by contributions from the entire Hα manifold. The laser-induced Hα fluorescence is estimated to be an order of magnitude stronger than the background Hα emission.

I. INTRODUCTION

Spatially and temporally resolved magnetic field ***B*** measurements have long been considered essential in plasma physics experiments. Coil or Hall probes inserted into the plasma are well-developed techniques, but not suitable for higher-temperature, low collisionality plasmas. Noninvasive spectroscopic techniques for field measurement, such as spontaneous emission from Zeeman-split levels, are difficult to perform at low field strengths and are also compromised by their line-integral nature. Modern, highly precise laser-induced fluorescence (LIF) techniques, including the motional Stark effect (MSE) diagnostic [1], can provide point, line, and sheet [two-dimensional (2D)] information, but generally only at high field strengths.

The quantum optics phenomenon of coherent population trapping (CPT) has been used in various studies, including laser cooling of atoms [2], electromagnetically induced transparency [3], and testing of the Jaynes-Cummings model of quantum chromodynamics [4]. CPT has recently been successfully used to make point measurements of magnetic fields in a neon discharge [5] and a sodium atomic vapor [6]. By taking advantage of the polarization states of the emission, magnetic-field direction can also be determined. Neon, sodium, and similar higher-Z species ionize quickly out of their lower states, hence, trace quantities would not be useful for field measurements in hot hydrogen plasmas. Herein, we will examine if neutral hydrogen, although at small concentrations in hot plasmas, could be used in CPT experiments to determine the local ***B***.

In semiclassical atom-field theory, for a single laser, the most efficient frequency for optical pumping of an electron from a lower to an upper level occurs when the laser frequency equals the frequency difference between those two levels or $\omega_{\text{Laser}} = (E_{\text{upper}} - E_{\text{lower}})/\hbar$. However, in a Λ system (Fig. 1), when two lasers are resonant with the two (greater) transitions, the optical electron may become "trapped" in a particular coherent superposition of the lower states and no pumping to the upper state will occur. For a collection of Λ-system atoms, exposure to the two lasers may quickly transition all electrons into that particular coherent superposition of lower

states, depleting the upper-state population and causing the fluorescence to vanish. The resulting spectroscopic condition is known as a "dark state." This is the essence of the CPT phenomenon: atomic quantum states can become coupled such that their populations can not be transferred to other states by certain resonant fields.

Hydrogen, the simplest element in the Universe with known and exact analytical solutions for its quantum mechanical wave functions, nevertheless, has a complex spectroscopy. Its lines are closely spaced and the effect of hyperfine structure is often much stronger for atomic hydrogen than for other atoms. Yet, due to its relevance toward realizing fusion reactors, quantifying magnetic fields in hydrogen plasma experiments is critical. As such, the objective of this study is to examine the CPT phenomenon applied to neutral atomic hydrogen, including the effects of fine and hyperfine splitting, Doppler broadening, and ionization fraction, toward evaluating its possible utility as a magnetic-field diagnostic.

One plasma configuration that would benefit from development of a CPT-based magnetic-field diagnostic is the field-reversed configuration (FRC), as illustrated in Fig. 2. The FRC has no toroidal magnetic field, and both plasma and magnetic field exist on its major axis. It has the highest β (ratio of plasma pressure to magnetic-field energy density) of any potential fusion device and the simplest geometry, fitting inside a cylindrical vacuum vessel and employing only external solenoidal ring magnets. Higher β means higher temperature, stable plasmas are possible, allowing use of fuels that produce far fewer neutrons than D-T [7], hence alleviating radiation problems. Currents flowing in the toroidal direction (dashed lines), in combination with the external ring magnets, create the closed field line shape. The magnetic field is zero at the two X points and along the O-point line (minor magnetic axis). The field strength required for FRC confinement is less than for lower-β configurations, such as tokamaks, obviously much lower near the minor axis, a null. In this paper, we will explore whether the CPT technique applied to hydrogen is suitable for measuring the low magnetic field ($<$0.1 T) of the FRC's interior.

In the following, CPT will be formulated for application to the atomic hydrogen $3p$-$2s$ transition states (Hα emission),
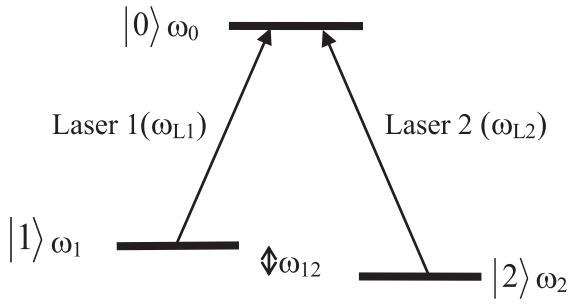
FIG. 1. Schematic of Λ system. Upper state $|0\rangle$ has energy $\hbar\omega_0$, and lower states $|1\rangle$ and $|2\rangle$ $\hbar\omega_1$ and $\hbar\omega_2$, respectively, relative to the atomic ground state. The applied lasers have frequencies ω_{L1} and ω_{L2}. The frequency difference between the lasers is ω_{12}.

including considering the effects of fine (electron spin-orbit) and hyperfine (nuclear spin-orbit) structure, and Doppler broadening.

II. THEORY

A. Coherent population trapping: The Bloch equations

A combined formalism from Arimondo and Orriols [8], Orriols [9], and Aspect *et al.* [10] will be used in deriving CPT applied to a three-level "Lambda" system shown in Fig. 1. Quantum state $|0\rangle$ is the upper state, while $|1\rangle$ and $|2\rangle$ are the lower states with energies $E_0 > E_1 \approx E_2$ (relative to the atomic ground state). Lower states $|1\rangle$ and $|2\rangle$ could be the Zeeman-split states for the present purposes. Two lasers are assumed, each producing an electromagnetic field with tunable frequency.

The quantum mechanical noninteracting Hamiltonian including kinetic and internal energies is

$$H_0 = \frac{p^2}{2m} + \sum_j E_j |j\rangle\langle j| = \frac{p^2}{2m} + \hbar \sum_j \omega_j |j\rangle\langle j|, \quad (1)$$
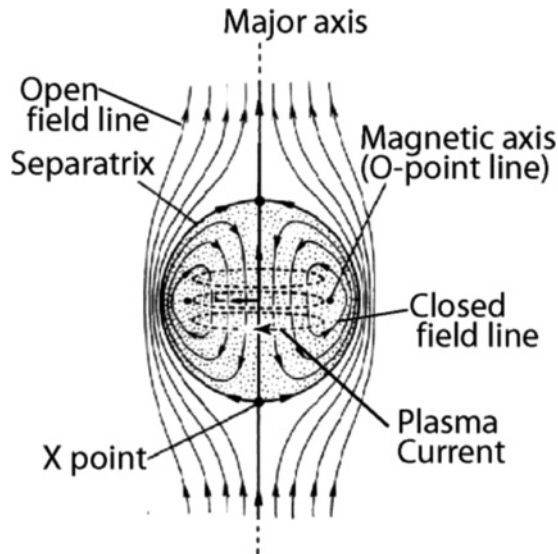

FIG. 2. FRC schematic. FRCs may be spherical, prolate, or oblate.

where the state vectors $|j\rangle$ are orthonormal ($j = 0,1,2$), p is the atom's momentum, and m its mass. The coupling Hamiltonian for electric dipole interaction with an electromagnetic field is

$$V = -\vec{D} \cdot \vec{E}(t), \quad (2)$$

where $\vec{D}$ is the electric dipole vector operator and $\vec{E}$ is the classical electric field. The combined electromagnetic field for two laser beams propagating in the z direction can be written as

$$\vec{E}(t) = \tfrac{1}{2}\vec{\varepsilon}_1 \xi_1 \exp[i(k_1 z - \omega_{L1}t) + \text{c.c.}]$$
$$+ \tfrac{1}{2}\vec{\varepsilon}_2 \xi_2 \exp[i(\pm k_2 z - \omega_{L2}t + \Phi) + \text{c.c.}], \quad (3)$$

where $\vec{\varepsilon}_j$ is the polarization vector, ξ_j is the electric field strength, k_j is the wave number, ω_{Lj} is the frequency of laser j, Φ is the relative phase of the beams, and c.c. represents the complex conjugate. The $\pm$ symbol designates whether the beams are copropagating ($+$) or counterpropagating ($-$). For circularly polarized beams, $\vec{\varepsilon}_j = \mp(e_x \pm ie_y)/\sqrt{2}$ corresponding to σ^+ or σ^- polarization, respectively, or $\vec{\varepsilon}_j = e_z$ for linear π polarization, where e_x, e_y, and e_z are Cartesian unit vectors of the laboratory reference frame. Assuming the laser fields connect the lower states to the upper $|0\rangle$ state, the Rabi frequencies Ω_j for each laser beam 1 and 2 can be defined as

$$\Omega_1 = -\frac{\xi_1}{\hbar} e^{i\theta_1} \langle 0 | \vec{\varepsilon}_1 \cdot \vec{D} | 1 \rangle, \quad (4a)$$

$$\Omega_2 = -\frac{\xi_2}{\hbar} e^{i\theta_2} \langle 0 | \vec{\varepsilon}_2 \cdot \vec{D} | 2 \rangle. \quad (4b)$$

Note that the Rabi frequencies can be complex if circularly polarized beams are used, and that the beam phase difference Φ is incorporated into θ_2. Combining Eqs. (3) and (4) into the interaction Hamiltonian of Eq. (2) and invoking the rotating-wave approximation [11] gives

$$V = \frac{\hbar}{2}[|\Omega_1|e^{-i(\omega_{L1}t-\theta_1)}|0\rangle\langle 1| \exp(ik_1 z)$$
$$+ |\Omega_2|e^{-i(\omega_{L2}t-\theta_2)}|0\rangle\langle 2| \exp(\pm ik_2 z) + \text{H.c.}], \quad (5)$$

where H.c. is the Hermitian conjugate. Using the relation for photons of momentum $\pm\hbar k$ [10]

$$\exp(\pm ikz) = \sum_p |p\rangle\langle p \mp \hbar k| \quad (6)$$

and from hereafter omitting the magnitude symbol for the Rabi frequencies, the final form for the interaction Hamiltonian is

$$V = \frac{\hbar}{2}\sum_p [\Omega_1 e^{-i(\omega_{L1}t-\theta_1)}|0,p\rangle\langle 1, p-\hbar k_1|$$
$$+ \Omega_2 e^{-i(\omega_{L2}t-\theta_2)}|0,p\rangle\langle 2, p \mp \hbar k_2| + \text{H.c.}]. \quad (7)$$

The upper state $|0,p\rangle$ can only be coupled to ground states $|1, p-\hbar k_1\rangle$ and $|2, p \mp \hbar k_2\rangle$ such that the summation in Eq. (7) reduces to just these coupling terms.

The Heisenberg equations of motion (Bloch equations) for the state population densities ρ_{jj} and coherences ρ_{jk} ($j \neq k$) are derived through the Von Neumann commutation relation

$$\frac{\partial \rho}{\partial t} = \frac{1}{i\hbar}[H_0 + V, \rho]. \quad (8)$$

Using Eqs. (1) and (7) in Eq. (8), nine (including complex conjugates) linear first-order ordinary differential equations are obtained as

$$\dot{\rho}_{00} = \frac{i}{2}[\Omega_1 e^{+i(\omega_{L1}t-\theta_1)}\rho_{01} + \Omega_2 e^{+i(\omega_{L2}t-\theta_2)}\rho_{02}$$
$$- \Omega_1 e^{-i(\omega_{L1}t-\theta_1)}\rho_{01}^* - \Omega_2 e^{-i(\omega_{L2}t-\theta_2)}\rho_{02}^*], \quad (9a)$$

$$\dot{\rho}_{11} = \frac{i}{2}[\Omega_1 e^{-i(\omega_{L1}t-\theta_1)}\rho_{01}^* - \Omega_1 e^{+i(\omega_{L1}t-\theta_1)}\rho_{01}], \quad (9b)$$

$$\dot{\rho}_{22} = \frac{i}{2}[\Omega_2 e^{-i(\omega_{L2}t-\theta_2)}\rho_{02}^* - \Omega_2 e^{+i(\omega_{L2}t-\theta_2)}\rho_{02}], \quad (9c)$$

$$\dot{\rho}_{01} = \frac{i}{2}\left[2\rho_{01}\left(-\omega_{01} - \frac{pk_1}{m} + \frac{\hbar k_1^2}{2m}\right)\right.$$
$$\left. + \Omega_1 e^{-i(\omega_{L1}t-\theta_1)}(\rho_{00} - \rho_{11}) - \Omega_2 e^{-i(\omega_{L2}t-\theta_2)}\rho_{12}^*\right], \quad (9d)$$

$$\dot{\rho}_{02} = \frac{i}{2}\left[2\rho_{02}\left(-\omega_{02} \mp \frac{pk_2}{m} + \frac{\hbar k_2^2}{2m}\right)\right.$$
$$\left. + \Omega_2 e^{-i(\omega_{L2}t-\theta_2)}(\rho_{00} - \rho_{22}) - \Omega_1 e^{-i(\omega_{L1}t-\theta_1)}\rho_{12}\right], \quad (9e)$$

$$\dot{\rho}_{12} = \frac{i}{2}\left[2\rho_{12}\left(-\omega_{12} + \frac{p(k_1 \mp k_2)}{m} - \frac{\hbar(k_1^2 - k_2^2)}{2m}\right)\right.$$
$$\left. + \Omega_2 e^{-i(\omega_{L2}t-\theta_2)}\rho_{01}^* - \Omega_1 e^{+i(\omega_{L1}t-\theta_1)}\rho_{02}\right], \quad (9f)$$

where $\rho_{kj}^* = \rho_{jk}$ ($j \neq k$), $\omega_{jk} = \omega_j - \omega_k$, pk/m is the frequency correction due to nonzero atomic velocities (Doppler shifting), $\hbar k^2/2m$ is the atomic recoil frequency shift resulting from photon absorption, and the upper signs refer to copropagating laser beams and lower sign for counterpropagating. While the recoil velocity may be important for laser cooling of atoms, for the photon wavelengths of this study (656 nm), this term is negligibly small at ≈ 1 MHz. The atomic velocity is $\upsilon = p/m$. Note that numerical values for frequencies will be quoted in Hz rather than s^{-1}.

Relaxation processes, including collisional effects and spontaneous emission, should be added to Eqs. (9) [12,13]. In this paper, applicable to low-density hydrogen plasma, collisions are rare such that these effects in the relaxation terms are not needed. Denote the spontaneous emission rates as Γ_0, Γ_1, and Γ_2 for the $|0\rangle$, $|1\rangle$, and $|2\rangle$ states, respectively. The relaxation rate for decoherence rate between the $|1\rangle$ and $|2\rangle$ states, Γ_{12}, is determined by the transit time $1/\Gamma_t = r_L/\upsilon$ of the atom in the electromagnetic laser field, a beam of radius r_L for the present purposes. Note that $1/\Gamma_t$ would depend on collisions if the collision rate were of the same order or greater than r_L/υ. With these relaxation terms included, Eqs. (9) can be written as

$$\dot{\tilde{\rho}}_{00} = -\Gamma_0\tilde{\rho}_{00} + \frac{i}{2}[\Omega_1(\tilde{\rho}_{01} - \tilde{\rho}_{01}^*) + \Omega_2(\tilde{\rho}_{02} - \tilde{\rho}_{02}^*)], \quad (10a)$$

$$\dot{\tilde{\rho}}_{11} = \frac{\Gamma_0}{2}\tilde{\rho}_{00} - \Gamma_1\tilde{\rho}_{11} + \frac{i}{2}\Omega_1(\tilde{\rho}_{01}^* - \tilde{\rho}_{01}), \quad (10b)$$

$$\dot{\tilde{\rho}}_{22} = \frac{\Gamma_0}{2}\tilde{\rho}_{00} - \Gamma_2\tilde{\rho}_{22} + \frac{i}{2}\Omega_2(\tilde{\rho}_{02}^* - \tilde{\rho}_{02}), \quad (10c)$$

$$\dot{\tilde{\rho}}_{01} = -\frac{\Gamma_0}{2}\tilde{\rho}_{01} + i\left[\delta_{L1}\tilde{\rho}_{01} + \frac{\Omega_1}{2}(\tilde{\rho}_{00} - \tilde{\rho}_{11}) - \frac{\Omega_2}{2}\tilde{\rho}_{12}^*\right], \quad (10d)$$

$$\dot{\tilde{\rho}}_{02} = -\frac{\Gamma_0}{2}\tilde{\rho}_{02} + i\left[\delta_{L2}\tilde{\rho}_{02} + \frac{\Omega_2}{2}(\tilde{\rho}_{00} - \tilde{\rho}_{22}) - \frac{\Omega_1}{2}\tilde{\rho}_{12}\right], \quad (10e)$$

$$\dot{\tilde{\rho}}_{12} = -\Gamma_{12}\tilde{\rho}_{12} + i\left(\delta_R\tilde{\rho}_{12} + \frac{\Omega_2}{2}\tilde{\rho}_{01}^* - \frac{\Omega_1}{2}\tilde{\rho}_{02}\right), \quad (10f)$$

where $\delta_{L1} = (1 - \upsilon/c)\omega_{L1} - \omega_{01}$ and $\delta_{L2} = (1 \mp \upsilon/c)\omega_{L2} - \omega_{02}$ are the laser detuning parameters from resonance between the $|0\rangle$ and $|1\rangle$, and $|0\rangle$ and $|2\rangle$ states, respectively, and $\delta_R = \delta_{L2} - \delta_{L1} = \Delta\omega_L - \omega_{12} + \frac{\upsilon}{c}(\omega_{L1} \mp \omega_{L2})$ is the Raman two-photon detuning parameter. Note that the Doppler effect is implicit in the Raman detuning parameter through the υ/c term.

To eliminate the oscillating terms of Eqs. (9), the variable substitutions $\tilde{\rho}_{0j} = \rho_{0j}e^{i(\omega_{Lj}t-\theta_j)}$, $\tilde{\rho}_{12} = \rho_{12}e^{i(\Delta\omega_L t-\Delta\theta)}$, $\tilde{\rho}_{jj} = \rho_{jj}$, $\tilde{\rho}_{kj}^* = \tilde{\rho}_{jk}$ ($j \neq k$) were used, where $\Delta\omega_L = \omega_{L2} - \omega_{L1}$ and $\Delta\theta = \theta_2 - \theta_1$. The index of refraction $N = kc/\omega = 1$ was assumed since the plasma and electron cyclotron frequencies are negligibly small compared with ω in the present experiments (an electron density above $n_e \sim 10^{18}$ cm^{-3} and a magnetic field above 100 Tesla are needed for the plasma frequency and electron cyclotron frequency, respectively, to affect the refractive index at the planned laser frequencies).

The critical criterion for establishing CPT is δ_R. When δ_R equals zero, the $|1\rangle$ and $|2\rangle$ states become strongly coupled, atoms become trapped in a coherent superposition of the lower states, and pumping to the $|0\rangle$ state ceases. Note that the laser detuning parameters δ_{Lj} need not equal zero to achieve CPT, but rather their difference must equal zero, which is equivalent to $\delta_R = 0$. Physically, this means that the lasers can be detuned from pumping the $|0\rangle$ state, even rather significantly, but their frequency difference (including the Doppler-shift correction) must equal the beat frequency between the two lower $|1\rangle$ and $|2\rangle$ states to cause CPT.

For the low hydrogen temperatures considered here (less than 1 eV), υ/c is $\sim 10^{-4}$ such that the Doppler-shift factor in δ_R has a negligible effect for copropagating laser beams (minus sign in δ_R) since $|\omega_{L1} - \omega_{L2}| \approx \omega_{12} \approx \Delta\omega_L$, resulting in a less than 1 MHz frequency correction to the detuning parameter. The Doppler shift will be important for CPT resonance only for multi-keV temperatures in copropagating beam experiments. However, the Doppler effect can not be neglected in counterpropagating beam experiments since the frequency correction could then be appreciable ($\omega_{L1} + \omega_{L2} \gg \omega_{12}, \Delta\omega_L$). This is the impetus for achieving velocity-selective CPT resonance in counterpropagating beam experiments since the lasers can be detuned to exactly match the desired atomic velocity. In other words, utilizing the Doppler effect as a velocity diagnostic with CPT is analogous to using the Zeeman shift herein as a magnetic-field diagnostic.

Therefore, measurements using the CPT effect will be Doppler-free for copropagating dual laser beams, and atomic

velocity distributions, whether Maxwellian or otherwise, do not need to be considered. The velocity terms will be neglected in δ_{Lj} and δ_R, for the present purposes and, correspondingly, Eqs. (10) do not depend on the atomic velocities.

III. RESULTS

A. Experimental parameters for hydrogen

To study the effects of CPT in a warm hydrogen plasma, appropriate values for the parameters in Eqs. (10) are needed. The Rabi frequencies depend on the $H\alpha$ transition dipole moment and the laser field amplitude through Eq. (4). The dipole moment is estimated as $|\vec{D}| \approx a_0 e$, where a_0 is the hydrogen Bohr radius. The laser electric field strength $|\vec{\xi}|$ is given by

$$|\vec{\xi}| = \left(\frac{2}{c} \frac{P}{\pi r_L^2} \right), \tag{11}$$

where P is the laser power, and c is the speed of light. Assuming a laser power of 300 mW and beam radius of 1 mm, the Rabi frequency will be $\Omega_R \approx 700$ MHz. The optimal Rabi frequency to minimize power broadening while maximizing magnetic-field detectability is given by a critical frequency as $\Omega_{\text{crit}}^2 = \Gamma_0 \Gamma_t$ [14]. Using relevant relaxation parameters (see below), $\Omega_{\text{crit}} \sim 10$ MHz, above which no better detectability is achieved, but line broadening worsens.

In the proposed Λ system for the hydrogen $H\alpha$ emission (Fig. 1), states $|0\rangle$, $|1\rangle$, and $|2\rangle$ represent the $|3p_{1/2}; m' = +1/2\rangle$ and the metastable $|2s_{1/2}; m'' = \pm 1/2\rangle$ states, respectively. (This choice will be discussed in more detail in the following.) The convention of a single prime for upper states and double primes for lower states will be followed. The spontaneous emission rates for these states are 22.45 MHz [15] for Γ_0 and 8.23 Hz [16] for Γ_1 and Γ_2 in the absence of electric fields and collisional deexcitation (to be discussed later).

The decoherence rate Γ_{12}, representing the relaxation of coherence between the two lower states of the Λ system, is an important parameter for CPT, as higher rates lead to weaker CPT effects [9,13]. As discussed earlier, Γ_{12} can be considered the rate at which atoms leave either of the lower states, and is the sum of a collisional relaxation rate and a transit relaxation rate [12,17]. The average H-atom collisional relaxation rate is $\Gamma_{\text{Coll}} = \upsilon_T / \lambda_{\text{mfp}} \sim 10^4$ Hz, where υ_T is the atomic thermal velocity, T = 0.4 eV, λ_{mfp} is the atomic mean-free path, and $p = 1.2$ mTorr for the hydrogen plasma of the PFRC-1 [18]. The average transit relaxation rate can be estimated as $\upsilon_T / r_L = 6.2$ MHz or $= 0.28\Gamma_0$. Therefore, the short transit time dominates, and $\Gamma_{12} \approx \upsilon_T / r_L$.

Because the $2s$ state is metastable, the coronal model [19] is not appropriate since population losses can be caused by both radiative emission and electron-impact excitation to higher levels during the $2s$ time scale. The rate equations for the $n = 2$ and 3 states, neglecting $n = 4$ and greater cascade transitions, can then be written as

$$\dot{n}_{2s} = n_1 n_e \langle \sigma_{1 \to 2s} \upsilon_e \rangle - n_{2s} n_e \langle \sigma_{2s \to 3} \upsilon_e \rangle - n_{2s} n_e \langle \sigma_{2s \to 1s} \upsilon_e \rangle$$
$$+ n_3 / \tau_{3 \to 2s} - n_{2s} / \tau_{2s}, \tag{12a}$$

$$\dot{n}_3 = n_1 n_e \langle \sigma_{1 \to 3} \upsilon_e \rangle + n_{2s} n_e \langle \sigma_{2s \to 3} \upsilon_e \rangle - n_3 / \tau_3, \tag{12b}$$

where n_1 is the $1s$ ground state density, n_{2s} is the $2s$ state density, and n_3 is the combined density of the $3s$, $3p$, and $3d$ states (the $2p$ state does not affect these populations in the coronal approximation). Similarly, $\tau_{3 \to 2s}$ is the relaxation time from the $n = 3$ state to the $2s$ state, τ_{2s} is the metastable lifetime of the $2s$ state, and τ_3 is the total lifetime of the $n = 3$ state. The electron-impact excitation (deexcitation) cross sections are represented as $\sigma_{i \to j}$ ($\sigma_{j \to i}$), and υ_e is the electron velocity. Using the excitation cross-section calculation method detailed by Sobel'man [20], the cross sections required are $\sigma_{1 \to 2s} = 5 \times 10^{-18}$ cm$^2 = \sigma_{2s \to 1}$ (by detailed balancing [20]), $\sigma_{1 \to 3} = 0.9 \times 10^{-17}$ cm^2, and $\sigma_{2s \to 3} = 6 \times 10^{-16}$ cm^2. Since τ_{2s} is large, this term in (12a) is neglected, and the steady-state populations can be calculated by setting the time-derivative terms to zero, resulting in $n_{2s} \sim 10^{11}$ cm^{-3} and $n_3 \sim 10^8$ cm^{-3}.

B. Stark effect on 2s level metastability

The linear Stark splitting of H-atom fine-structure levels (j levels) by a weak ($\ll 3000$ V/cm) dc electric field is given by the formula of Bethe and Salpeter [21]:

$$\Delta E_{\text{dc}}^{\text{Stark}} = \frac{3}{4} \sqrt{n^2 - \left(j + \frac{1}{2} \right)^2} \frac{nm}{j(j+1)} \xi_{\text{dc}},$$
$$m = -j, -j + 1, \ldots, + j. \tag{13}$$

Note that the electric field ξ_{dc} is in atomic units (1 V/cm = 15 620 a.u. such that ΔE is in units of cm^{-1}). The Lamb shift is not included in the above equation, but should be for $j = 1/2$ of s states ($l = 0$). In such a case, the above equation should be replaced with [14]

$$\Delta E_{\text{dc}}^{\text{Stark-Lamb}} = \frac{L}{2} \pm \frac{1}{2} \sqrt{L^2 + 4(n^2 - 1)(nm\xi_{\text{dc}})^2}, \tag{14}$$

where the $\pm$ corresponds to $m = \pm 1/2$. The Lamb shift equals $L = 1.0578$ GHz (0.03526 cm^{-1}) for the $2s_{1/2}$ state (lying above the otherwise degenerate $2p_{1/2}$ state, in the absence of external fields) and is 315 MHz (0.0105 cm^{-1}) for the $3s_{1/2}$ state.

From numerical calculations of dc Stark effect of the hydrogen $2s_{1/2}$ hyperfine level ($F = 0,1$) [22], the associated frequency shift scales as $1100 E^2_{\text{Stark}}$ (Hz cm^2/V^2). Accordingly, a 100 V/cm dc field, the maximum expected in the FRC based on $10 T_e \omega_{\text{pi}}/c$, where ω_{pi} is the ion plasma frequency, would shift the $2s_{1/2}$ hyperfine levels by ~ 10 MHz. Note, however, that the $\sim E^2$ correlation was taken from numerical simulations, which may not apply to higher field strengths than were measured in Ref. [14] ($\sim$mV/cm), or when magnetic fields are also present since magnetic- and electric-field effects can not be disentangled. Regardless, a nominal 10-MHz dc Stark shift is assumed to be a conservative approximation.

The ac Stark effect in the low-frequency ($\omega_{\text{ac}} \ll \omega_{\text{Stark}} = DE_{\text{Stark}}/\hbar$), low strength limit ($\alpha E^2_{\text{Stark}}/\hbar \ll \omega_{\text{ac}}$ where α is the electric polarizability) in a one-level atom [23] causes a frequency shift of $\sim \omega_{\text{Stark}}$. The polarizability can be estimated through $\alpha = n^6 + \frac{7}{4} n^4 (l^2 + l + 2)$ [15], expressed in atomic units (1.65×10^{-41} s^{4}A^2/kg), which for a $2s$ term is $\alpha_{2s} = 2 \times 10^{-39}$ s^{4}A^2/ kg, resulting in a characteristic ac

Stark *strength frequency* of just 7 Hz for a 15-V/cm field. In fact, electric-field amplitudes on the order of 10^4 V/cm would be needed to achieve a critical Stark strength of $\sim$1 MHz, such that for the ac frequencies and field amplitudes to be considered here, we will always be in the weak ac field regime. As detailed in Ref. [14], the hyperfine ac Stark shift is $\sim 10^{-6}$ that of the $1s - 2s$ ac Stark shifting, such that an overall ac Stark shift of 20 MHz, for a 15-V/cm field amplitude, for example, is reduced to the $\sim$Hz level in the hydrogen hyperfine structure. Therefore, ac Stark shifting will be considered negligible in the hyperfine structure, but dc Stark effects could cause a shift of $\sim$10 MHz in the $2s_{1/2}$ hyperfine levels.

External electric fields will quench the otherwise metastable $2s_{1/2}$ state of atomic hydrogen. As noted earlier, the relaxation rate Γ_{2s} of the $2s_{1/2}$ state in the absence of external field is 8.23 Hz [16], while the relaxation rate Γ_{2p} for the $2p$ states are 3.94 GHz [24]. An applied electric increases the $2s_{1/2}$ decay rate according to Lamb and Retherford's formula [25]

$$\Gamma_{\text{Stark}} = \Gamma_{2p} \frac{|\langle 2s_{1/2}|e\vec{E}\cdot\vec{r}|2p\rangle|^2}{\hbar^2\left(\omega^2 + \Gamma_{2p}^2/4\right)}, \tag{15}$$

where $e\vec{E}\cdot\vec{r}$ is the electric dipole moment between the $2s_{1/2}$ and $2p$ states, and ω is the frequency difference between the states. For large fields, Γ_{Stark} asymptotes to $\Gamma_{2p}/2$, consistent with the results of Rojansky and Van Vleck [26]. Metastability quenching thus scales quadratically with moderate electric field strength, as is observed experimentally. For the $2s_{1/2}$-$2p$ states, the frequency difference is 10 GHz. Assuming a radius of 2×10^{-8} cm for the electric dipole length scale for the $n = 2$ states, the quenched $2s_{1/2}$ decay rate is given by $\Gamma_{\text{Stark}} \sim 150E^2$ (Hz), where E is in units of V/cm. Thus, a 100-V/cm dc electric field causes an enhanced $2s_{1/2}$ decay rate of $\sim$1.5 MHz, faster than the wall collision frequency of 10^5 Hz. Such quenching greatly increases the $2s_{1/2}$ decay rate, but not nearly to the level of the $2p$ decay rate (627 MHz). Therefore, for a 100-V/cm field, the $2s_{1/2}$ state can still be considered largely metastable relative to the $2p$ states, even considering deactivation through wall collisions. Note that field strengths on the order of thousands V/cm are needed to approach the asymptotic regime where $\Gamma_{\text{Stark}} \sim \Gamma_{2p}/2$. This level of field would cause Stark shifts of the energy levels to become within range of the electron spin-orbit fine splitting, such that considering electric-field effects as a small perturbation becomes no longer valid.

Therefore, for larger fields, of the order 3000 V/cm and greater, the $2s_{1/2}$ state is fully quenched, losing all its metastability characteristics, and total angular momentum quantum number J (or equivalently F if considering hyperfine structure) is no longer a good quantum number, in addition to electron orbital angular momentum L not being good for all nonvanishing field strengths. Such high electric fields are not expected for the current generation of FRC plasma experiments, and will not be considered below.

C. Hα emission spectrum

In the absence of an applied magnetic field, the Hα spectrum has a center wavelength of 656 nm (4.57×10^{14} Hz), consisting

TABLE I. Fine and hyperfine splitting of Hα terms. The applied magnetic field which would cause the same splitting is also shown as B_{crit} [see (18)].

State	$\Delta\nu$ (MHz)	ΔE (10^{-8} eV)	B_{crit} (Gauss)
	Fine splitting		
$3d$	1086	449.7	776
$3p$	3252	1347	2323
$2p$	10997	4546	7843
	Hyperfine splitting		
$3d_{5/2}$	2.71	1.13	2
$3p_{3/2}$	7.03	2.91	5
$3d_{3/2}$	4.22	1.75	3
$3s_{1/2}$	52.77	21.86	38
$3p_{1/2}$	17.59	7.29	13
$2p_{3/2}$	23.74	9.83	17
$2s_{1/2}$	178.1	73.74	127
$2p_{1/2}$	59.39	24.58	42

of seven degenerate fine-electronic transitions. However, an external magnetic field will cause Zeeman splitting for each of the terms, resulting in 48 individual fine-electronic transitions. Fine splitting and hyperfine splitting of the terms involved in the Hα emission are shown in Table I. For low-magnetic-field diagnostics ($\sim$20 G), one must also account for hyperfine transitions, which would result in 136 individual electronic transitions.

The $3p_{1/2} \rightarrow 2s_{1/2}$ transitions were chosen for the best effectiveness in observing CPT due to the metastable $|2s\rangle$ state. The $3p_{1/2} \rightarrow s_{1/2}$ transitions are preferred to the $3p_{3/2} \rightarrow 2s_{1/2}$ transitions because the $m' = 1/2 \rightarrow m'' = 1/2$ transitions consist of just four Zeeman-split transitions, whereas the $m' = 3/2 \rightarrow m'' = 1/2$ transitions consist of six Zeeman-split transitions. Therefore, CPT will have a more significant effect on reducing fluorescence using the $3p_{1/2} \rightarrow 2s_{1/2}$ transitions than the $3p_{3/2} \rightarrow 2s_{1/2}$ transitions. The remaining five fine transitions of the manifold decay to the nonmetastable $2p$ state, with a spontaneous decay rate of 627 MHz [24]. In comparison with the 8.23-Hz decay rate (10^5 Hz including wall collisions) of the $2s$ states, the Λ systems using Zeeman-split $2p$ states as lower states are therefore not favorable for observing CPT effects.

Define ω_{01} as the frequency of the transition between the $|3p_{1/2}; m' = +1/2\rangle$ and $|2s_{1/2}; m'' = +1/2\rangle$ states, and ω_{02} as the frequency of the transition between the $|3p_{1/2}; m' = +1/2\rangle$ and $|2s_{1/2}; m'' = -1/2\rangle$ states. If two lasers are tuned to frequencies $\omega_{L1} = \omega_{01}$ and $\omega_{L2} = \omega_{02}$, then the Raman detuning parameter δ_R will be zero, the atoms will become trapped in the two lower states, and the radiative intensities of two of the four lines of the $3p_{1/2} \rightarrow 2s_{1/2}$ transition will be sharply reduced. If instead, ω_{L2} is fixed at ω_{02} ($\delta_{L2} = 0$) and ω_{L1} is scanned around ω_{01} (as in Fig. 3), then the observed light intensity will increase, and then drop to a minimum when $\omega_{L1} = \omega_{01}$. When the observed light intensity is at a minimum, one can then determine the magnetic-field strength using the difference in lower-state frequencies ($\omega_{12} = \Delta\omega_k$) from Zeeman splitting $\Delta\omega = g\mu_B B/\hbar$.
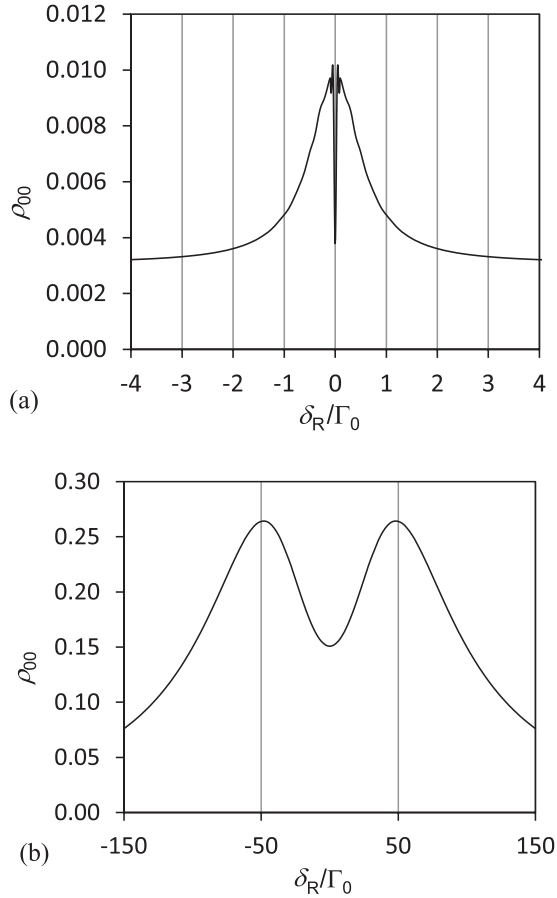
FIG. 3. Numerical solution of Eqs. (10) for ρ_{00} using (a) the idealized parameters of Orriols [9] and (b) Hα parameters for the $|3p_{1/2}; m' = +1/2\rangle \rightarrow |2s_{1/2}; m'' = \pm 1/2\rangle$ target transition. The FWHM of the dark line dip at $\delta_R = 0$ is $\sim 48\Gamma_0$, and $\Delta I = 0.43$ for (b).

The relative intensities of electronic transitions without line broadening are given by

$$I(n'\,j'm'|n''\,j''m'') \sim \rho_{00}(n'\,j'm')S(j'm'|j''m'')$$
$$\times A(n'\,j'm'|n''\,j''m'')h\nu_{n'j'm'\rightarrow n''j''m''},$$
(16)

where $I(n'\,j'm'|n''\,j''m'')$ is the line intensity (erg/cm^{3}s) from upper principal level n' with electron angular momentum quantum number $j'$and projection m' to lower state $n''\,j''m''$, $\rho_{00}(n'\,j'm')$ is the density of the excited state as calculated with Eqs. (10), A is the Einstein spontaneous decay rate, and $h\nu$ is the energy difference between the excited and lower states. S is the square of the Clebsch-Gordan coeffcient (Wigner $3j$ symbol) for electron orbital angular momentum transitions including Zeeman splitting [20].

The above hydrogen-relevant experimental parameters were used to solve Eqs. (10) for ρ_{00} in steady state for the isolated $|3p_{1/2}; m' = +1/2\rangle \rightarrow |2s_{1/2}; m'' = \pm 1/2\rangle$ Λ system, as shown in Fig. 3(b) [Fig. 3(a) shows an idealized CPT spectrum of Orriols [9]. The full width at half maximum (FWHM) of the dark line and the peak-to-valley per cent reduction in intensity $\Delta I = (I_{max} - I_{min})/I_{max}$, are metrics of the effectiveness of CPT. For the calculated CPT spectrum for hydrogen

plasma, the FWHM of the dark line is $\sim 48\Gamma_0$ (1.08 GHz), and the peak-to-valley reduction in intensity is $\Delta I = 0.43$. This idealized estimate shows that the CPT technique should work, in principle, as a magnetic-field diagnostic, but further refinements for actual conditions are needed.

Note that $\rho_{00}\left(n'\,j'm'\right)$ refers to the number density of excited *neutral* hydrogen atoms. In the PFRC-1, a balance between volumetric ionization and radiative recombination would cause the ratio of neutral hydrogen to electron densities R_H to be in the range $R_H = 10^{-6}$–10^{-7}, assuming $T_i = 0.4$ eV and $T_e = 100$–1000 eV. But, surface losses of ions to material structures in the PFRC-1 results in intense recycling, raising the measured value of R_H to $\sim$1. Later PFRC devices are expected to have far less recycling, hence lower R_H. If necessary, R_H could be increased by local gas puffing or neutral beam injection. Calculations with the DEGAS code [27] show that modest gas puffing could increase R_H to a steady-state value of 10^{-2} on axis and to 1 at the plasma separatrix.

D. Line broadening

For PFRC-1 parameters, Doppler broadening dominates over other line-broadening mechanisms. Assuming the atoms have a Maxwellian velocity distribution of width $\sigma_D = \nu_0\upsilon_T/c$, the Doppler-broadened intensity profile is [19]

$$I_D(\nu) = I(n'\,j'm'|n''\,j''m'')f_D(\nu - \nu_0),$$
(17a)

where

$$f_D(\nu - \nu_0) = \frac{1}{\sigma_D\sqrt{2\pi}}e^{-(\nu-\nu_0)^2/2\sigma_D^2}.$$
(17b)

Here, ν_0 denotes the line frequency $\nu_{n'j'm'\rightarrow n''j''m''}$ of Eq. (16). Doppler broadening completely blurs all the 48 fine and Zeeman-split electronic transitions if observed with a spectrometer, including the $3p_{1/2} \rightarrow 2s_{1/2}$ transitions (Fig. 4), as the FWHM of the Doppler broadening profiles at $T = 0.4$ eV is $\sqrt{8\ln2}\sigma_D \approx 22$ GHz. The frequency spacing between each
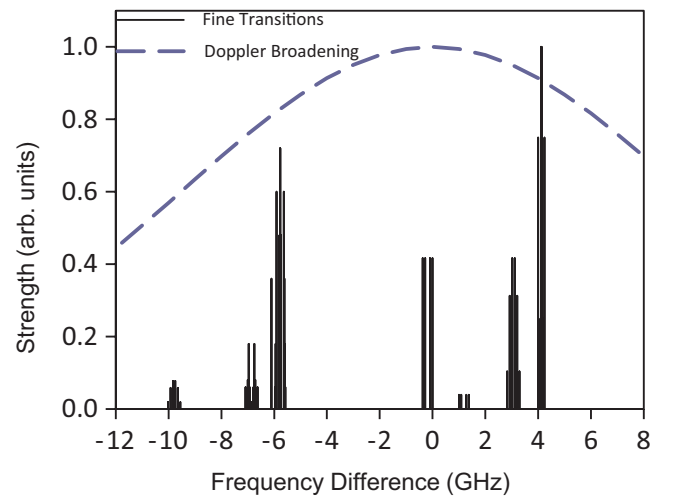

FIG. 4. (Color online) Strength and frequency (relative to target laser frequency of 457 THz) of 48 fine electronic transitions of Hα emission. Dashed blue line illustrates Doppler broadening centered at the 457-THz target frequency for a 0.4-eV hydrogen temperature (FWHM 22.2 GHz).

of the individual Zeeman-split $3p_{1/2} \rightarrow 2s_{1/2}$ transitions is ~100 MHz, two orders of magnitude less than the FWHM of Doppler broadening. Therefore, individual Zeeman-split transitions can not be resolved with a single-laser method but can be with the two-laser CPT approach we describe. All transitions of the Hα manifold must be considered.

E. CPT applied to the Hα manifold

Figure 3 illustrated the effects of CPT with relevant parameters for the Λ system constructed with the two $|3p_{1/2};m' = +1/2\rangle \rightarrow |2s_{1/2};m'' = \pm1/2\rangle$ transitions, without including other $n = 3 \rightarrow 2$ transitions. However, all transitions of the Hα manifold will be excited.

The observed fluorescence of the entire Hα manifold, including CPT effects, is

$$I_{\text{H}\alpha}(\nu) \sim \sum_{j',m'} \sum_{j'',m''} I(3j'm'|2j''m''), \qquad (18)$$

where appropriate dipole selection rules between $j'm' \rightarrow j''m''$ are followed. Implicit in Eq. (18) is the upper-state density $\rho_{00}(n' = 3, j'm')$ of Eq. (16), where ρ_{00} depends on the off resonance from the applied laser frequencies through δ_{L1} and δ_{L2}.

We will assume that one of the two propagating laser frequencies ω_{L2} is again set fixed to the $|3p_{1/2};m = +1/2\rangle \rightarrow |2s_{1/2};m = -1/2\rangle$ target transition, i.e., $\delta_{L2} = \omega_{L2} - \omega_{02} = 0$. The remaining laser frequency ω_{L1} will be allowed to vary throughout the bandwidth of the Doppler profile, thereby differentially pumping the upper-state populations of the various Hα terms, as well as causing some CPT resonance for nontarget transitions. All electronic transitions are approximated as Λ systems to account for partial CPT resonance of nontarget transitions. This assumption is not unreasonable since in 42 out of the 48 electronic transitions, the $|n = 3\rangle$ state decays to two $|n = 2\rangle$ states, making Λ systems. Each Λ system experiences different values for the laser detuning parameters δ_{L1} and δ_{L2}. The relative values of δ_{L1} and δ_{L2} for nontarget fine transitions when both lasers are tuned for the $|3p_{1/2};m = +1/2\rangle \rightarrow |2s_{1/2};m = \pm1/2\rangle$ target Λ system are shown in Table II. Resulting upper-state densities for two sample nontarget transitions are shown in Fig. 5, with δ_{L2} is set to zero for the $|3p_{1/2};m = +1/2\rangle \rightarrow |2s_{1/2};m = -1/2\rangle$ target transition, and δ_{L1} is allowed to vary.

TABLE II. Normalized effective laser detuning frequencies δ_{L1} and δ_{L2} for the eight fine-transition Λ systems when the two lasers are tuned for the target Λ system $|3p_{1/2};m' = +1/2\rangle \rightarrow |2s_{1/2};m'' = \pm1/2\rangle$. Frequencies are normalized by $\Gamma_0 = 22.5$ MHz.

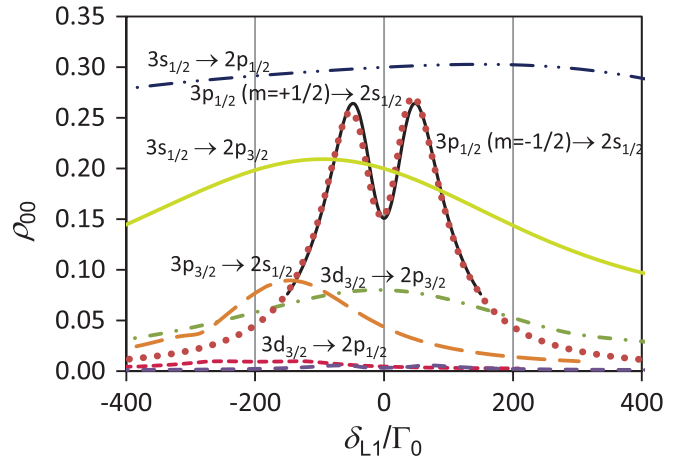| Λ system	δ_{L1}	δ_{L2}
$|3p_{1/2};m' = +1/2\rangle \rightarrow |2s_{1/2};m'' = \pm1/2\rangle$ (target)	0	0
$|3p_{1/2};m' = -1/2\rangle \rightarrow |2s_{1/2};m'' = \pm1/2\rangle$	-2	$+10$
$|3p_{3/2}\rangle \rightarrow |2s_{1/2}\rangle$	-149	-137
$|3s_{1/2}\rangle \rightarrow |2p_{1/2}\rangle$	-65	-53
$|3s_{1/2}\rangle \rightarrow |2p_{3/2}\rangle$	$+424$	$+436$
$|3d_{3/2}\rangle \rightarrow |2p_{3/2}\rangle$	$+293$	$+306$
$|3d_{5/2}\rangle \rightarrow |2p_{3/2}\rangle$	$+245$	$+258$
$|3d_{3/2}\rangle \rightarrow |2p_{1/2}\rangle$	-196	-183

FIG. 5. (Color online) CPT spectra of all seven fine-electronic transition Λ systems when the lasers are tuned for the target $|3p_{1/2};m' = +1/2\rangle \rightarrow |2s_{1/2};m'' = \pm1/2\rangle$ transitions. The CPT spectrum for the target transition $|3p_{1/2};m' = +1/2\rangle \rightarrow |2s_{1/2};m'' = +1/2\rangle$ is reproduced from Fig. 3 as the solid (black) line, and the $|3p_{1/2};m' = +1/2\rangle \rightarrow |2s_{1/2};m'' = -1/2\rangle$ transition is shown as a dotted (red) line closely following the solid line. The $|3d_{5/2}\rangle \rightarrow |2p_{3/2}\rangle$ transition is of low density and represented as the (blue) dashed line at the bottom of the graph (not labeled to avoid clutter).

To simplify the calculations, Zeeman splitting was ignored for the nontarget fine-electronic transitions since Zeeman splitting is small (~0.1 GHz) compared to frequency differences of electronic fine transitions (>1.4 GHz). With this assumption, the approximate Hα spectrum would consist of 4 $3p_{1/2} \rightarrow 2s_{1/2}$ Zeeman-split electronic transitions, 6 degenerate $3d_{3/2} \rightarrow 2p_{1/2}$ transitions, 6 degenerate $3p_{3/2} \rightarrow 2s_{1/2}$ transitions, 4 degenerate $3s_{1/2} \rightarrow 2p_{1/2}$ transitions, 12 degenerate $3d_{5/2} \rightarrow 2p_{3/2}$ transitions, 10 degenerate $3d_{3/2} \rightarrow 2p_{3/2}$ transitions, and 6 degenerate $3s_{1/2} \rightarrow 2p_{3/2}$ transitions (48 total transitions).
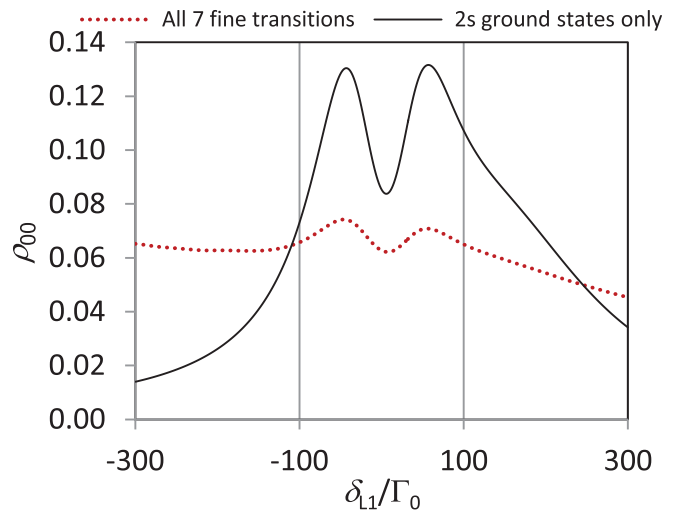

FIG. 6. (Color online) CPT numerical solution of upper state $n = 3$ density including all seven fine-electronic transitions (red, dashed line), and including just the fine-electronic transitions with metastable $2s$ ground states (black, solid line). The dark line FWHM is $48\Gamma_0$, but the frequency location of the dark line center is at $\delta_{L1} = -6\Gamma_0$.

Figure 6 shows the total fluorescence curve using Eq. (18), summing the curves of Fig. 5, versus laser tuning parameter δ_{L1}. In Fig. 6, the lower curve (red, dashed line) accounts for the effects of all seven fine electronic transitions in the Hα manifold. The FWHM of the total fluorescence curve is $\sim 48\Gamma_0$, similar to the FWHM of the fluorescence curve in Fig. 3, but ΔI decreases to 14%, compared to 43%. A notable feature is that the minimum value of the fluorescence is shifted away from $\delta_{L1} = 0$. The local minimum value for the fluorescence intensity in Fig. 6 occurs at $\delta_{L1} = -6\Gamma_0$ (-135 MHz) due to the addition of all the nontarget laser-pumped upper-state densities.

Another reasonable assumption is to ignore the effects of the $|n=3\rangle \rightarrow |2p\rangle$ transitions on the fluorescence curves since the decay from the $|2p\rangle$ states (~ 1 ns) is rapid compared to the long-lived $|2s\rangle$ metastable states. The $|2p\rangle$ states will therefore have lower densities than the $|2s\rangle$ states. Ignoring the effects of the $|n=3\rangle \rightarrow |2p\rangle$ transitions on the fluorescence curves results in slightly stronger CPT effects as illustrated by the upper (black, solid) curve in Fig. 6, which only includes the $|n=3\rangle \rightarrow |2s\rangle$ transitions. The FWHM of this curve remains at $\sim 48\Gamma_0$, but ΔI improves to 40%, closer to the value of ΔI in the idealized fluorescence curve in Fig. 3 ($\Delta I = 43\%$). Nevertheless, even assuming equal contributions from the $|2p\rangle$ and $|2s\rangle$ states, CPT effects still result in a discernible "dark line" in the fluorescence spectrum.

F. Measuring the magnetic-field strength

The magnetic-field strength can be measured using the changes in the fluorescence intensity due to CPT effects. The dark line in the fluorescence spectrum occurs when the Raman detuning parameter δ_R equals zero. Since $\delta_R = \delta_{L2} - \delta_{L1} = \Delta\omega_L - \omega_{12}$, the laser frequency difference when $\delta_R = 0$ is equal to the Zeeman splitting such that the magnetic field strength can be calculated through

$$B = \frac{\hbar \Delta \omega_L}{g \mu_B}, \qquad (19)$$

where g is the dimensionless magnetic moment and μ_B is the Bohr magneton. Equation (19) is accurate when $B \gg \Delta E_{\mathrm{HF}}/\mu_B$, where ΔE_{HF} is the hyperfine-splitting energy (see Table I). For low-strength magnetic fields (~ 20 G), the present CPT analysis has to be modified to include the effects of hyperfine splitting.

However, if the dark line is shifted from $\delta_R = 0$ due to the effect of multiple Λ systems being simultaneously excited due to Doppler broadening (as in Fig. 6), then measuring the magnetic-field strength is more difficult. For example, in Fig. 6, the local minimum in fluorescence is shifted, and is observed when $\delta_R = 6\Gamma_0 \approx 135$ MHz. This shift is roughly the same order as the Zeeman splitting between the $|2s_{1/2}; m = \pm 1/2\rangle$ states, which is ≈ 280 MHz. Such predicted frequency shifts must be taken into account when performing measurements.

It is of particular importance to note that no Hα CPT dark line will be observable with a spectrometer due to Doppler broadening of the fluorescence blurring the resonance. However, the transmitted spectrally integrated intensity through a band-pass filter centered on the Hα transition would show a dip at resonance *per* Fig. 6.

IV. DISCUSSION

Using the above theoretical estimates, a practical CPT experiment can be devised, as shown in Fig. 7 applied to the PFRC-1. A tunable laser beam is split with half the beam energy entering an Acousto-optical modulator (AOM). The frequency-shifted output from the AOM is then combined with the other half of the split beam. This combined, bichromatic beam is collimated and enters a fiber-optic coupler (FOC) to be routed through a polarization maintaining fiber to the PFRC-1 device. CCD cameras with a band-pass filter centered at the Hα emission of 656-nm frequency and ~ 20 GHz wide, are positioned to obtain fluorescence images resulting from laser illumination of the plasma column.

The frequency shift $\Delta\omega_L$ can be incrementally changed through adjusting the tunable laser frequency and the AOM to span the magnetic-field range of interest. The CCD arrays are oriented to view the desired cross section, and are triggered to coincide with each $\Delta\omega$. Because CPT affects only those atoms in resonance with the applied $\Delta\omega$, most of the pixels of the 2D image will record the background Hα emission caused by the $T_e \sim 150$ eV (appropriate for the PFRC-1) electron impact, but those pixels corresponding to regions of resonance with $\Delta\omega$ will register relatively lower total intensity due to the integrated dips in the fluorescence spectrum. Thus, by inverting these CCD images, the bright portions of each image will represent the magnetic-field strength as given by $B = \hbar\Delta\omega_L/g\mu_B$.

The procedure for making magnetic strength measurements is illustrated in Fig. 8. Computer simulation results for a 25-cm-radius FRC plasma is shown in Fig. 8(a), showing 100-G isocontour lines in the r-z plane. Assume for this example that the AOM has been set for a frequency shift corresponding to this 100-G magnetic strength. According to CPT theory described above, there would be $\sim 40\%$ less fluorescence emitted from the regions of the plasma illuminated by the laser sheet having magnetic strengths corresponding to this frequency shift. As such, dark lines would be seen, as has
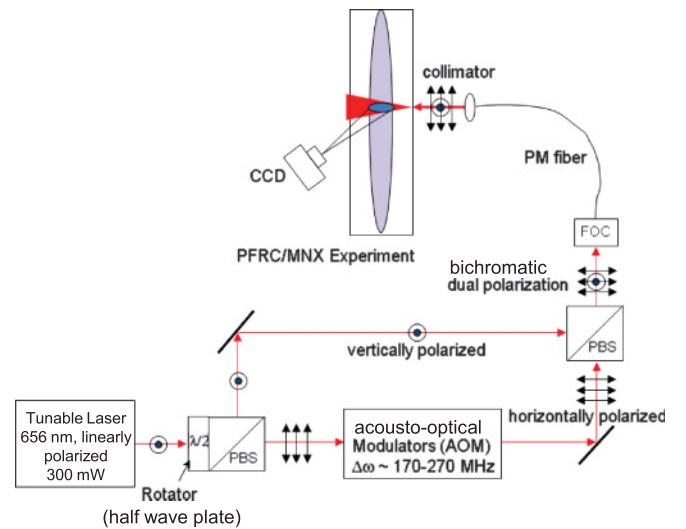

FIG. 7. (Color online) Experimental setup for magnetic-field measurements using CPT showing laser system, polarizing beam splitter (PBS), acousto-optical modulator (AOM), fiber-optic coupler (FOC), and polarizations.
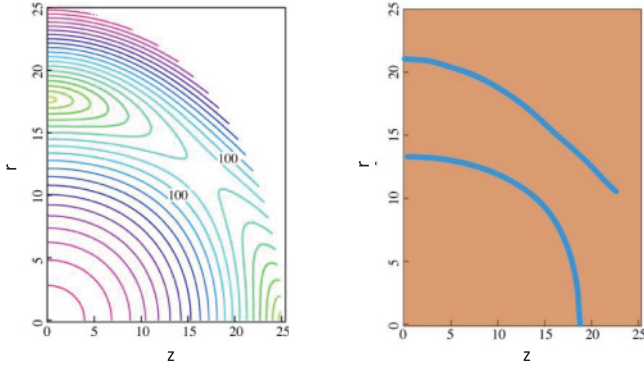
FIG. 8. (Color online) (a) Illustration of 2D magnetic strength isocontours from a computer simulation of a 25-cm-radius spherical FRC. The X-point null is at $z = 25$ cm and $r = 0$. The O-point null is at $z = 0$ and $r = 17.7$ cm. (b) A 2D image showing the "dark lines" resulting from CPT tuned to 100-G field identified.

been illustrated in Fig. 8(b). These dark lines give a direct 2D measurement of geometry of the magnetic strengths having the prescribed value selected through the AOM. The background color of Fig. 8(b) is meant to represent the fluorescence recorded from the rest of the laser-sheet cross section, which is relatively intense since there is no population trapping for the regions not at the CPT resonance. Images such as Fig. 8(b) can be captured at a time scale set by the upper-state relaxation time, which is ∼0.05 ms. The Alfvén time for the hydrogen plasma is of order 1 ms, such that sequential images similar to Fig. 8(b) would show near-real-time evolution of the magnetic-field topology.

As discussed earlier, the minimum Rabi frequency needed to achieve CPT is given by a critical frequency $\Omega_{\mathrm{crit}}^2 = \Gamma_0 \Gamma_t \sim$ 10 MHz for the PFRC-1 experiment. For a laser power of 300 mW and a 2-mm-diameter beam cross section, the laser intensity is ∼10 W/cm^2, giving a laser excitation Rabi frequency of $\Omega \sim 700$ MHz. The proposed experiments are therefore well above the threshold criterion for establishing CPT, and the laser power could be lowered if desired. However, lower laser power would also reduce the photons available at the detector, which will now be discussed.

For resonant scattering, where radiation is absorbed at the resonant frequency ω_0 of the transition of interest and then reemitted as fluorescence at the same frequency, the photon intensity is given by [28]

$$I_D = \eta \frac{\Omega}{4\pi} \frac{g_u}{g_l + g_u} \frac{\chi}{\chi + 1} V \frac{n_l}{\tau}, \qquad (20)$$

where I_D is the photon count rate collected by the detector, η is the detector efficiency, Ω is the solid angle of the emission (not to be confused with the Rabi frequency Ω_j), g_u and g_l are the upper- and lower-state degeneracies, respectively, V is the measurement volume, n_l is the absorbing state density, and τ is the radiative lifetime of the upper state (i.e., $\tau = \tau_3$). The saturation parameter χ is given by

$$\chi = I(\omega_0) \frac{g_l + g_u}{g_l} \frac{\pi c^2}{2\hbar \omega_0^3} L(\omega_0), \qquad (21)$$

where $I(\omega_0)$ is the incident laser intensity (W/cm^2) and $L(\omega_0)$ is the spectral line broadening at ω_0. The resonant absorption cross section $\sigma_{\mathrm{res}} = \hbar \omega B_{\mathrm{E}} L(\omega)/c$ (here, B_{E} is the Einstein absorption coefficient) is included within χ. Note that when the incident radiant intensity is weak, such that χ is small, the detected intensity increases linearly with incident radiant intensity, but when χ is large, I_D saturates such that no further signal can be detected no matter how much more radiant intensity is applied.

Since the Doppler width will be much larger than the natural linewidth for the atomic hydrogen temperatures considered here (∼0.4 eV), the line-shape function is Gaussian, and therefore at resonance the value of $L(\omega_0)$ is the Doppler width, which corresponds to 45 ps for 656 nm radiation and a H temperature of 0.4 eV. For the Hα transition ($n = 3 \rightarrow 2$), the degeneracy of the upper state is 36 and 16 for the lower state, giving a saturation parameter of $\chi = 0.083 I(\omega_0)$. For a laser intensity $I(\omega_0) \sim 10$ W/cm^2, $\chi \sim 0.83$, which is the linear regime, resulting in $I_D = 0.3\eta(\Omega/4\pi)V n_l/\tau_3$.

For single-frequency-laser-beam fluorescence, the absorbing state density n_l will be a fraction of the full n_{2s} density since only those Doppler-shifted atoms in resonance with one of the 136 allowed hyperfine transitions can take part in the excitation process. With a 10-MHz laser linewidth, this means that ∼1.4 GHz of the 22-GHz Doppler-broadened profile (see Fig. 4) is in resonance such that $n_l \sim n_{2s}/20$.

Using the previously calculated density of the hydrogen 2s level of ∼10^{11} cm^{-3} and lifetime of the $n = 3$ level ($\tau_3 = 5.6$ ns), and assuming a 16-mm, $f/1.4$ lens in front of a $\eta = 50\%$ CCD with 20-μm pixels at a standoff distance of ∼20 cm (2.6×10^{-3} ster), the photon rate collected by each pixel viewing the beam is ∼10^{10} photons/s from resonant scattering of a 10-W/cm^2, 656-nm laser beam through a plasma consisting of 10^{12} cm^{-3} of electrons at 150 eV, and hydrogen atoms at a density of 10^{12} cm^{-3}. Over an Alfvén time of ∼1 μs, therefore, ∼10^4 photons/pixel viewing the illuminated volume will recorded by the CCD. Assuming photon counting obeys Poisson statistics, the signal to noise recorded per pixel is S/N ∼ 100. Therefore, sufficient signal should be received by the detector to rise above the noise during an Alfvén time. Also, pixels could be binned to achieve greater S/N, which would also be advantageous to allow higher speed imaging of the CCD, but would degrade the imaging resolution. For example, 10×10 binning of pixels would increase the detected photon counts by a factor of 100, thereby increasing the S/N to ∼1,000, while only degrading the image resolution down to ∼2 mm, which is certainly tolerable for the present purposes. The background Hα emission intensity is $I_{\mathrm{back}} = \eta \frac{\Omega}{4\pi} V \frac{n_3}{\tau_3} \sim$ 10^9 photons/s. Thus, the resonant fluorescence signal should be an order of magnitude stronger than the background Hα emission.

We have shown that applying CPT as a magnetic-field diagnostic is feasible theoretically, using practical parameters for a FRC magnetic fusion device. Fine and hyperfine levels of the Hα transition manifold have been considered in the analysis, and their excitation due to finite Doppler width. Stark effects, both dc and ac, will be negligible effects for the plasma parameters of FRC devices, but could become important for dc electric fields much larger than 1000 V/cm. The Zeeman effect

will cause overlap of fine transition lines of the Hα manifold beginning at field strengths of ∼350 G, which will complicate the spectral structure of the Hα fluorescence. However, this does not necessarily mean that CPT can only be applied to low-strength magnetic fields, but further refinement of the present analysis may be needed. For fields lower than about 20 G, hyperfine transitions should be included in the analysis for a more precise estimation of CPT effects, but this should be a second-order effect of the fine transition analysis presented here.

[1] F. Levinton, Rev. Sci. Instrum. **70**, 810 (1999).

[2] G. Morigi, B. Zambon, N. Leinfellner, and E. Arimondo, Phys. Rev. A **53**, 2616 (1996).

[3] S. E. Harris, Phys. Today **50**(7), 36 (1997).

[4] D. Jonathan, K. Furuya, and A. Vidiella-Barranco, J. Mod. Opt. **46**, 1697 (1999).

[5] R. Akhmedzhanov, I. Zelensky, R. Kolesov, and E. Kuznetsova, Phys. Rev. E **69**, 036409 (2004).

[6] H. Asahi, K. Motomura, K. Harada, and M. Mitsunaga, Opt. Lett. **28**, 1153 (2003).

[7] J. M. Dawson, in *Fusion B*, edited by E. Teller (Academic, New York, 1981), p. 453.

[8] E. Arimondo and G. Orriols, Lett. Nuovo Cimento **17**, 333 (1976).

[9] G. Orriols, Nuovo Cimento **53**, 1 (1979).

[10] A. Aspect, E. Arimondo, R. Kaiser, N. Vansteenkiste, and C. Cohen-Tannoudji, J. Opt. Soc. Am. B **6**, 2112 (1989).

[11] C. Cohen-Tannoudji, B. Diu, and F. LaLoe, *Quantum Mechanics* (Wiley-Interscience, Paris, 2006).

[12] E. Arimondo, Phys. Rev. A **54**, 2216 (1996).

[13] E. Arimondo, in *Progress in Optics*, edited by E. Wolf (Elsevier, Amsterdam, 1996), Vol. 35, p. 257.

[14] Fleischhauer and M. O. Scully, Phys. Rev. A **49**, 1973 (1994).

[15] Y. Ralchenko, A. Kramida, J. Reader, and NIST ASD Team, NIST Atomic Spectra Database v3.1.5 [http://physics.nist.gov/asd3].

[16] J. Shapiro and G. Breit, Phys. Rev. **113**, 179 (1959).

[17] F. Renzoni and E. Arimondo, Phys. Rev. A **58**, 4717 (1998).

[18] D. R. Farley, D. P. Stotler, D. P. Lundberg, and S. A. Cohen, J. Quant. Spectrosc. Radiat. Transfer **112**, 800 (2010).

[19] I. H. Hutchinson, *Principles of Plasma Diagnostics*, 2nd ed. (Cambridge University Press, Cambridge, 2002), p. 223.

[20] I. I. Sobel'man, L. A. Vainshtein, and E. A. Yukov, *Excitation of Atoms and Broadening of Spectral Lines 2nd Ed.* (Springer, Berlin, 1995), Chaps. 5,6.

[21] H. A. Bethe and E. E. Salpeter, *Quantum Mechanics of One-and Two-Electron Atoms* (Plenum, New York, 1977).

[22] N. Kolachevsky, M. Fischer, S. G. Karshenboim, and T. W. Hänsch, Phys. Rev. Letts. **92**, 033003 (2004).

[23] N. B. Delone and V. P. Krainov, Uspekhi Fizicheskikh Nauk **169**, 772 (1999).

[24] L. C. Green, P. P. Rush, and C. D. Chandler, Astrophys. J. Suppl. Ser. **3**, 37 (1957).

[25] W. E. Lamb and R. C. Retherford, Phys. Rev. **79**, 549 (1950).

[26] V. Rojansky and J. H. Van Vleck, Phys. Rev. **32**, 327 (1928); V. Rojansky, *ibid*. **33**, 1 (1929).

[27] D. Stotler and C. Karney, Contrib. Plasma Phys. **34**, 392 (1994); Michael Oake (private communication).

[28] K. Muraoka and M. Maeda, *Laser-Aided Diagnostics of Plasma and Gases* (IOP Publishing, Bristol, 2001), Chap. 2.